Applied and Computational Mechanics 19 (2025) 49–68

Applied and Computational Mechanics

Dynamic behaviour of rotating functionally graded Timoshenko beam via B-spline collocation method

S. Chichkhede[a], D. Mahapatra[b], S. Sanyal[a], S. Bhowmick[a,*]

[a] *Department of Mechanical Engineering, National Institute of Technology, Raipur 492011, India*
[b] *Department of Agriculture Engineering, Indira Gandhi Krishi Vishwavidyalaya, Raipur 492011, India*

Received 3 March 2025; accepted 19 June 2025

Abstract

The dynamic behaviour of a rotating Timoshenko functionally graded (FG) beam is investigated, with material properties varying along the height of the beam according to a power-law distribution. The study investigates how key parameters such as the power-law index, rotational speed, slenderness ratio, and various functionally graded material (FGM) compositions affect the dynamic response of the beam. The governing equations, which incorporate shear deformation and rotary inertia effects, are formulated and solved using the B-spline collocation method. The results provide critical insights into how these parameters affect the natural properties of FG beams, contributing to optimization and development for the design of advanced rotating structures in engineering applications.

Keywords: dynamic analysis, Timoshenko rotating beam, functionally graded beam, power index, B-spline collocation method

1. Introduction

Functionally graded materials (FGMs) are designed to have a smooth and gradual change in their properties by varying the composition or structure throughout the material. This unique feature allows different qualities, such as wear resistance, oxidation resistance, stiffness, and thermal durability, to be placed exactly where they are needed most. This helps to improve the overall performance of the material. In rotating beams, such as those found in turbine blades, helicopter rotors, or other high-speed machinery, FGMs provide significant benefits. Rotating beams are subjected to complex loading conditions, including mechanical loads and strong centrifugal forces from rotation. These forces can create high stress in certain areas, which can lead to failure. FGMs help manage these stresses more effectively, making structures stronger and more reliable.

Traditional homogeneous materials often fail to provide the right balance required to withstand diverse and challenging conditions faced by rotating beams. To address this, researchers have explored FGMs in detail. In the widely acclaimed work [13], the author introduced a new method to analyse functionally graded beams with rotary inertia and shear deformation, deriving a fourth-order equation to express physical quantities and presenting results for static deflection, stress distribution, flexural waves, free vibration, natural frequencies, and mode shapes of different beam configurations. Nguyen et al. [14] studied rectangular FG beams under axial loads using first-order shear deformation theory. They examined how factors such as the power-law

*Corresponding author. E-mail: sbhowmick.mech@nitrr.ac.in.
https://doi.org/10.24132/acm.2025.986

index, material differences, and Poisson ratio affect displacements, stresses, vibration frequencies, buckling loads, and mode shapes. In [1], Almitani et al. focused on the stress and vibration analysis of rotating FG beams, exploring how the material gradation and the rotational speed impact their performance. Thomas et al. [20] analysed how FG beams behave at large amplitudes during rotation, particularly looking at hardening and softening effects at different speeds. These studies highlight the unique advantages of FGMs in managing the demands of rotating beams.

In [22], Zghal et al. studied functionally graded porous beams with an emphasis on parameters such as porosity distribution, gradient index, slenderness ratio, and boundary conditions, affecting natural frequencies, stiffness, and vibration control. The recent study on functionally graded beams by Kılıç and Özdemir [12] explored the effects of porosity, gradient index, boundary conditions, and material properties on vibration, buckling, and stability, using advanced finite element methods. The study by Bouzidi et al. [3] used the finite element method to analyse dynamic behaviour of functionally graded rotor-blade systems. Key findings included improved natural frequencies, stability, and efficiency over their metallic counterparts at varying speeds and gradients. In [11], Karahan and Özdemir analysed vibration of functionally graded blades using the finite element method. Results confirmed the accuracy of the model, showing that rotational speed increases natural frequencies, while material gradient and slenderness ratio significantly impact the vibration behaviour.

Chen et al. [4] developed a floating frame reference model for rotating functionally graded beams, incorporating effects of centroid and neutral axes. Key findings revealed that steady bending deformation increases with angular speed, influencing vibration characteristics minimally. In [10], Hao-Nan et al. analysed rotating axially graded tapered Timoshenko beams using the Chebyshev-Ritz method, revealing significant impacts of rotational speed, taper ratios, and material gradients on natural frequencies. The paper by Panchore and Ganguli [17] presented a quadratic B-spline finite element method for analysing free vibrations of rotating non-uniform Euler-Bernoulli beams, demonstrating improved accuracy and reduced computational effort compared to conventional methods, particularly for the first few natural frequencies.

The study by Ebrahimi and Mokhtari [6] used the differential transformation method to analyse free vibrations of rotating Mori-Tanaka-based functionally graded beams, revealing significant influences of material gradation and rotational speed on natural frequencies. In the article [8], Fang and Zhou utilised the Chebyshev-Ritz method to analyse free vibrations of rotating axially functionally graded tapered Timoshenko beams, highlighting the significant impact of material properties and geometric factors on natural frequencies. Ebrahimi and Mokhtari [7] studied the free vibrations of rotating exponentially functionally graded Timoshenko beams using the differential transform method, revealing significant effects of material gradation and rotational speed on natural frequencies. The paper by Özdemir [15] explored the vibration characteristics of rotating functionally graded Timoshenko beams using the differential transform method. Key findings included the effects of material distribution, slenderness ratio, and rotational speed on natural frequencies.

The paper by Ebrahimi and Dashti [5] examined free vibration of rotating non-uniform functionally graded beams. The study revealed that increasing the rotational speed and hub radius raises the natural frequencies of functionally graded beams, while higher power-law exponents decrease them. The breadth-taper ratio impacts frequencies more prominently than the height-taper ratio. In [21], Wattanasakulpong et al. studied free vibration in functionally graded beams using an improved shear deformation theory and validated results experimentally. Findings showed increased frequencies with higher stiffness and denser material composition. Piovan

and Sampaio [18] investigated the dynamic behaviour of rotating functionally graded beams. Results revealed increased geometric stiffening with ceramic-rich surfaces, while metal-rich cores experienced greater oscillatory axial displacements under acceleration changes. In [19], Şimşek made a fundamental frequency analysis of functionally graded beams under various boundary conditions using higher-order beam theories. Results highlighted the frequency reduction with increased power-law exponent and the significance of slenderness ratio. Ozdemir Ozgumus and Kaya [16] analysed vibrations in rotating tapered Timoshenko beams. Results revealed increasing rotational speed and hub radius enhanced natural frequencies, while slenderness ratio inversely affected higher modes. The work by Gunda and Ganguli [9] presented rational interpolation functions for analysing rotating beams, accounting for centrifugal stiffening effects. The results showed an improved accuracy in predicting natural frequencies compared to classical finite element methods, especially at higher rotational speeds.

This work provides the basis for the mathematical formulation of a functionally graded beam using the B-spline collocation method, which uses piecewise polynomials to approximate function, to ensure continuity and smoothness up to a certain degree depending on the order of the spline. The aim of the study is to determine the effect of material grading, rotational speed, slenderness ratio, and different material compositions on the natural frequency of the rotating beam. The study forms the foundation for further advanced investigations in many applications such as turbine blades, aerospace structures etc. However, the modelling and treatment of such application cases shall demand to incorporate additional fields in the formulation from the associated mechanics/physics of such applications, namely thermal and flow-around-blades fields.

2. Governing equations

Let us consider a beam of length L, width b, and height h. The beam is fixed to a hub of radius R and the hub is free to rotate about the vertical axis, as illustrated in Fig. 1 (left). The hub rotates with an angular velocity $\Omega\,[\mathrm{rad\,sec}^{-1}]$. The beam is functionally graded, with its material properties varying along the height (transverse direction) based on a power-law distribution, as shown in Fig. 1 (right). The FG beam has a metal-rich composition at the top surface and a

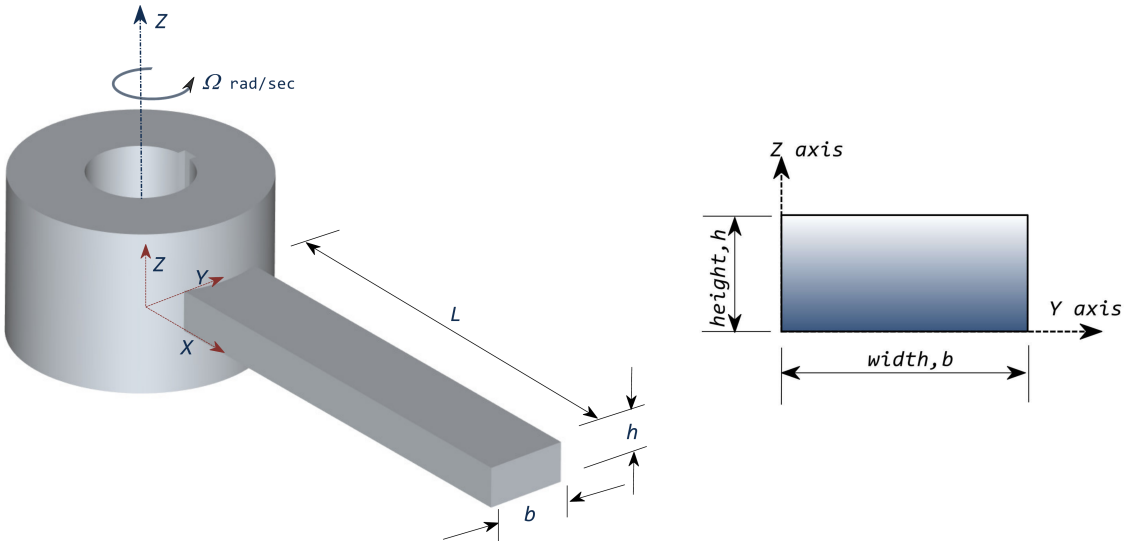

Fig. 1. Rotating functionally graded cantilever beam (*left*) and its cross-section (*right*)

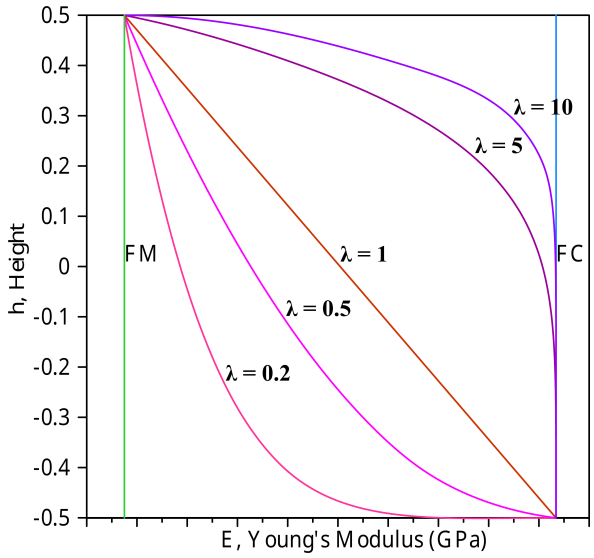

Fig. 2. Variation of the Young's modulus along the height of the FG beam

ceramic-rich composition at the bottom surface. The volume fractions of ceramic V_c and metal V_m component vary along the z-direction following the power-law relations given as

$$V_c = \left(\frac{z}{h} + \frac{1}{2}\right)^{\lambda}, \tag{1}$$

$$V_m = 1 - V_c \tag{2}$$

with the power-law index $\lambda \geq 0$. The effective material properties are evaluated using the rule of mixture given by

$$P(z) = P_c V_c + P_m V_m. \tag{3}$$

Using (3), the Young's modulus E and the density ϱ can be written as

$$E(z) = (E_T - E_B)\left(\frac{z}{h} + \frac{1}{2}\right)^{\lambda} + E_B, \tag{4}$$

$$\varrho(z) = (\varrho_T - \varrho_B)\left(\frac{z}{h} + \frac{1}{2}\right)^{\lambda} + \varrho_B, \tag{5}$$

$$G(z) = \frac{E(z)}{2(1+\mu(z))}, \tag{6}$$

where μ is the Poisson's ratio. The symbols T and B refer to the top and bottom surfaces of the beam, which consist of metal and ceramic materials, respectively. The corresponding Young's moduli at these surfaces are denoted by E_T and E_B. The variation of the Young's modulus along the beam height is illustrated in Fig. 2. The shear correction factor k is given by [13]

$$k(z) = \frac{5\big(1+\mu(z)\big)}{6+5\mu(z)}. \tag{7}$$

The Hamilton's principle is employed to derive the governing equations for the dynamic analysis of the rotating FG beam. As per this principle, for a system subjected to conservative

forces, the actual motion between two arbitrary time instants t_1 and t_2 makes the time integral

$$I = \int_{t_1}^{t_2} L \, \mathrm{d}t \tag{8}$$

stationary, i.e., an extremum. The Lagrangian function L in (8) is defined as the difference between the kinetic energy K and the total potential energy, which includes U_0 and U_R, i.e.,

$$I = \int_{t_1}^{t_2} \left[K - (U_0 + U_R) \right] \mathrm{d}t. \tag{9}$$

For a rotating beam, the total potential energy $U_0 + U_R$ consists of the internal strain energy and of the work done by the centrifugal force.

The expression for the kinetic energy is obtained considering the geometry and material properties as mentioned above. The position vector $\vec{r}$ of a point P on the beam is given as

$$\vec{r} = (R + x + u)\vec{i} + (y + v)\vec{j} + (z + w)\vec{k}, \tag{10}$$

where u, v, and w are the displacement components, representing displacements along the x-, y-, and z-axes, respectively. The displacement field is defined as follows

$$u(x, z) = u_0(x) + z\theta, \qquad v(x, z) = 0, \qquad w(x, z) = x(x). \tag{11}$$

In this context, u_0 and θ represent the axial displacement and rotation of the midplane, respectively. Then, the velocity vector $\vec{v}$ can be derived as

$$\vec{v} = \left[-\Omega(y + v) + \frac{\partial u}{\partial t} \right] \vec{i} + \left[\Omega(R + x + u) + \frac{\partial v}{\partial t} \right] \vec{j} + \left[\frac{\partial w}{\partial t} \right] \vec{k}. \tag{12}$$

The expression for the kinetic energy is formulated based on the Timoshenko beam theory

$$K = \frac{1}{2} \int_V \varrho(z) \vec{v} \cdot \vec{v} \, \mathrm{d}V, \tag{13}$$

$$\delta K = \int_0^L \int_A \varrho \left[\left(\frac{\partial u_0}{\partial t} + z \frac{\partial w}{\partial t} \right)^2 + \left(\frac{\partial w}{\partial t} \right)^2 + \Omega^2 \left(R + x + u_0 + z\theta \right)^2 \right] \mathrm{d}A \, \mathrm{d}x. \tag{14}$$

Solving the inner integral and after some modifications, equation (14) can be rewritten into the following form:

$$\begin{aligned} \delta K = \int_0^L \Bigg\{ & \varrho_0 \left[\frac{\partial u_0}{\partial t} \frac{\partial \delta u_0}{\partial t} + \frac{\partial w}{\partial t} \frac{\partial \delta w}{\partial t} + \Omega^2 \left(R + x + u_0 \right) \delta u_0 \right] + \\ & \varrho_1 \left[\frac{\partial u_0}{\partial t} \frac{\partial \delta \theta}{\partial t} + \frac{\partial \theta}{\partial t} \frac{\partial \delta u_0}{\partial t} + \Omega^2 \left(R + x + u_0 \right) \delta \theta + \Omega^2 \theta \delta u_0 \right] + \\ & \varrho_2 \left[\frac{\partial \theta}{\partial t} \frac{\partial \delta \theta}{\partial t} + \Omega^2 \theta \delta \theta \right] \Bigg\} \mathrm{d}x, \end{aligned} \tag{15}$$

where $[\varrho_0, \varrho_1, \varrho_2] = \int_A \varrho(z)[1, z, z^2]\,\mathrm{d}A$. Integrating (15) between t_1 and t_2 yields

$$\delta K = \int_{t_1}^{t_2}\int_0^L \Bigg\{ \varrho_0 \left[-\frac{\partial^2 u_0}{\partial t^2}\delta u_0 - \frac{\partial^2 w}{\partial t^2} + \Omega^2 \left(R + x + u_0\right)\delta u_0 \right] + \varrho_1 \left[-\frac{\partial^2 u_0}{\partial t^2}\delta\theta - \frac{\partial^2 \theta}{\partial t^2}\delta u_0 + \Omega^2 \left(R + x + u_0\right)\delta\theta + \Omega^2\theta\delta u_0 \right] + \varrho_2 \left[-\frac{\partial^2 \theta}{\partial t^2}\delta\theta + \Omega^2\theta\delta\theta \right] \Bigg\}\,\mathrm{d}x\,\mathrm{d}t. \tag{16}$$

To derive the total potential energy $U_0 + U_R$, the strain components need to be determined first. Based on the moderate deformation theory, the normal strain ε_{xx} and shear strain γ_{xz} are expressed accordingly

$$\varepsilon_{xx} = \frac{\partial u_0}{\partial x} + \frac{1}{2}\left(\frac{\partial w}{\partial x}\right)^2 + z\frac{\partial \theta}{\partial x}, \qquad \gamma_{xz} = \frac{\partial w}{\partial x} + \theta. \tag{17}$$

Then, the corresponding strain energy δU_0 can be formulated as

$$\delta U_0 = \int_0^L \int_A \left(\sigma_{xx}\delta\varepsilon_{xx} + \tau_{xz}\delta\gamma_{xz}\right)\,\mathrm{d}A\,\mathrm{d}x, \tag{18}$$

$$\delta U_0 = \int_0^L \left\{ N_{xx}\,\delta\left[\frac{\partial u_0}{\partial x} + \frac{1}{2}\left(\frac{\partial w}{\partial x}\right)^2\right] + M_{xx}\frac{\partial \theta}{\partial x} + Q\,\delta\left(\frac{\partial w}{\partial x} + \theta\right)\right\}\,\mathrm{d}x, \tag{19}$$

where

$$N_{xx} = b\int_{-\frac{h}{2}}^{\frac{h}{2}} \sigma_{xx}\,\mathrm{d}z, \qquad M_{xx} = b\int_{-\frac{h}{2}}^{\frac{h}{2}} z\sigma_{xx}\,\mathrm{d}z, \qquad Q = b\int_{-\frac{h}{2}}^{\frac{h}{2}} \tau_{xz}\,\mathrm{d}z. \tag{20}$$

The external work δU_R done by the centrifugal force N_R on the beam is given by

$$\delta U_R = \frac{1}{2}\int_0^L N_R\left(\frac{\partial w}{\partial x}\right)^2\,\mathrm{d}x, \qquad \delta U_R = -\int_0^L \frac{\partial}{\partial x}\left(N_R\frac{\partial w}{\partial x}\right)\delta w\,\mathrm{d}x, \tag{21}$$

while the centrifugal force is defined as

$$N_R = \int_x^L \int_A \varrho\Omega^2(R + \xi)\,\mathrm{d}A\,\mathrm{d}\xi, \qquad N_R = \varrho A\Omega^2\left[R\left(L - x\right) + \frac{L^2 - x^2}{2}\right]. \tag{22}$$

By substituting (16), (19), and $(21)_2$ into (9), and further differentiating the obtained relation, we get

$$\delta u_0: \qquad \frac{\partial N_{xx}}{\partial x} + \varrho_0\Omega^2(R + x + u_0) + \varrho_1\Omega^2\theta = \varrho_0\frac{\partial^2 u_0}{\partial t^2} + \varrho_1\frac{\partial^2 \theta}{\partial t^2}, \tag{23}$$

$$\delta\theta: \qquad \frac{\partial M_{xx}}{\partial x} - Q + \varrho_1\Omega^2(R + x + u_0) + \varrho_2\theta\Omega^2 = \varrho_1\frac{\partial^2 u_0}{\partial t^2} + \varrho_2\frac{\partial^2 \theta}{\partial t^2}, \tag{24}$$

$$\delta w: \qquad \frac{1}{2}\frac{\partial}{\partial x}\left(N_{xx}\frac{\partial w}{\partial x}\right) + \frac{\partial Q}{\partial x} - \frac{\partial}{\partial x}\left(N_R\frac{\partial w}{\partial x}\right) + q = \varrho_0\frac{\partial^2 w}{\partial t^2}. \tag{25}$$

By solving (23)–(25), we get the equations of motion as

$$\hat{E}_2\frac{\partial^2\theta}{\partial x^2} - G_0\left(\theta + \frac{\partial w}{\partial x}\right) + \hat{\varrho}_2\Omega^2\theta = \hat{\varrho}_2\frac{\partial^2\theta}{\partial t^2}, \tag{26}$$

$$\frac{\partial}{\partial x}\left[G_0\left(\theta + \frac{\partial w}{\partial x}\right)\right] - \frac{\partial}{\partial x}\left(N_R\frac{\partial w}{\partial x}\right) + q = \varrho_0\frac{\partial^2 w}{\partial t^2}, \tag{27}$$

where

$$\hat{\varrho}_2 = \varrho_2 - \frac{\varrho_1^2}{\varrho_0}, \quad \hat{E}_2 = E_2 - \frac{E_1^2}{E_0}, \quad [E_0, E_1, E_2] = \int\limits_A E(z)[1, z, z^2]\,\mathrm{d}A. \tag{28}$$

The quantity G_0 in (26)–(27) follows from $(20)_3$ as

$$Q = b\int\limits_{-\frac{h}{2}}^{\frac{h}{2}} \tau_{xz}\,\mathrm{d}z = b\int\limits_{-\frac{h}{2}}^{\frac{h}{2}} k_s G_0\gamma_{xz}\,\mathrm{d}z, \tag{29}$$

where k_s denotes the shear correction factor. The boundary conditions for (26)–(27) can be formulated as

$$w\big|_{x=0} = 0, \qquad \left.\frac{dw}{dx}\right|_{x=0} = 0, \qquad M\big|_{x=L} = 0, \qquad \left.\frac{dM}{dx}\right|_{x=L} = 0.$$

The term $\hat{\varrho}_2\Omega^2\theta$ in (26) is significant at higher speed only and, therefore, it can be omitted following [2]. Further, according to the paper [13], it can be written

$$w = F - \frac{\hat{E}_2}{G_0}\frac{\partial^2 F}{\partial x^2} + \frac{\hat{\varrho}_2}{G_0}\frac{\partial^2 F}{\partial t^2} \quad \text{and} \quad \theta = -\frac{\partial F}{\partial x}, \tag{30}$$

where F is an auxiliary function. Therefore using (30), a single equation is obtained from (26)–(27) in the form

$$\left(\hat{E}_2 - \frac{\hat{E}_2 N_1}{G_0}\right)\frac{\partial^4 F}{\partial x^4} - \frac{N_2\hat{E}_2}{G_0}\frac{\partial^3 F}{\partial x^3} + N_1\frac{\partial^2 F}{\partial x^2} + N_2\frac{\partial F}{\partial x} - \left(\hat{\varrho}_2 + \frac{\hat{E}_2\varrho_0}{G_0} - \frac{N_1\hat{\varrho}_2}{G_0}\right)\frac{\partial^4 F}{\partial x^2\partial t^2} + \varrho_0\frac{\partial^2 F}{\partial t^2} + \frac{N_2\hat{\varrho}_2}{G_0}\frac{\partial^3 F}{\partial x\partial t^2} + \frac{\varrho_0\hat{\varrho}_2}{G_0}\frac{\partial^4 F}{\partial t^4} = 0. \tag{31}$$

Considering a simple harmonic function, the auxiliary function F takes the form of

$$F = f(x)e^{i\omega t}. \tag{32}$$

Substituting (32) into (31), the final equation for the FG beam is obtained as

$$\left(\hat{E}_2 - \frac{\hat{E}_2 N_1}{G_0}\right)\frac{\partial^4 f}{\partial x^4} + \frac{N_2\hat{E}_2}{G_0}\frac{\partial^3 f}{\partial x^3} + \left[\left(\hat{\varrho}_2 + \frac{\hat{E}_2\varrho_0}{G_0} + \frac{N_1\hat{\varrho}_2}{G_0}\right)\omega^2 - N_1\right]\frac{\partial^2 f}{\partial x^2} + \left(\frac{N_2\hat{\varrho}_2\omega^2}{G_0} - N_2\right)\frac{\partial f}{\partial x} + \left(\frac{\varrho_0\hat{\varrho}_2}{G_0}\omega^4 - \varrho_0\omega^2\right)f = 0. \tag{33}$$

By applying a suitable numerical technique to solve (33), the auxiliary function F can be obtained, which is then used to compute other dependent variables. In this study, equation

(33) is solved using the collocation method with B-spline basis functions as the approximating functions.

The B-spline collocation method yields a closed-form, piecewise continuous solution, where the differential equation is enforced at a finite set of points known as collocation points. The parametric coordinate t determines the polynomial order, referred to as the knot vector. An open-type knot vector T is assumed in this formulation and is defined by the following expression:

$$T = [t_0, t_1, t_2, \ldots, t_{n+k+1}], \tag{34}$$

where $n+1$ represents the number of control points, and k denotes the order of the polynomial spline. Once the knot vector is established, the B-spline basis functions $N_{i,k}(t)$ are defined recursively using the Cox-de Boor recursion formula

$$\begin{aligned} N_{i,1}(t) &= \begin{cases} 1 \text{ for } x_i \leq t \leq x_{i+1}, \\ 0 \text{ otherwise}, \end{cases} \\ N_{i,k}(t) &= \frac{(t - x_i) N_{i,k-1}(t)}{x_{i+k-1} - x_i} + \frac{(x_{i+k} - t) N_{i+1,k-1}(t)}{x_{i+k} - x_{i+1}}. \end{aligned} \tag{35}$$

The resulting B-spline curve is constructed using the $n+1$ control points $B_0, B_1, B_2, \ldots, B_n$ along with the corresponding basis functions and is expressed as

$$F(t) = \sum_{i=1}^{n+1} B_i N_{i,k}(t),$$

where t and k in (35) lie in the following intervals:

$$t_{\text{min}} \leq t \leq t_{\text{max}}, \qquad 2 \leq k \leq n+1. \tag{36}$$

The function F is substituted into the governing equation as an approximating polynomial in such a way that it satisfies the specified boundary conditions. Since the number of unknowns in the approximating polynomial exceeds the number of boundary conditions, the solution must be enforced at specific discrete points known as collocation points. In this work, the collocation (or abscissa control) points are determined using the Grevillea abscissa method. The position vector of the control point B_i, which defines the B-spline curve with respect to the parametric coordinate t, is calculated as follows

$$x_i = \frac{1}{n} \left(t_i + t_{i+1} + \ldots + t_{i+n-1} \right). \tag{37}$$

As B-splines offer a larger control over the spread and behaviour of the approximating functions, the degree of polynomial plays an important role in improving the precision of the results. The results are only *accurate* at the knots and *precise* at the remaining positions of the beam/geometry span. Higher degree of polynomials results in obtaining the better accuracy at the knots and better precision all over the span. Collocation methods (using regular polynomial approximations), in general, amongst the other methods of weighted residuals, are by far the easiest and mostly less accurate of the lot. The best of the precision is reported to be obtained by the Galerkin's error minimisation technique and/or the least squares method. But the mathematics involved in these methods are not as simple as those of the collocation method. At this point, the B-spline collocation method comes into the picture. A method that, by virtue of using

Table 1. Properties of constituents of FGM

FGM constituents	Young's modulus E [GPa]	Density $\varrho\,[\mathrm{kg\,m^{-3}}]$	Poisson's ratio
Aluminium	70	2707	0.3
Alumina	380	3960	0.3
Steel	210	7850	0.3

B-splines as approximating functions instead of regular polynomials, offers a larger number of knots/collocation points where the residual error may be forced to zero (thus, increasing the accuracy comparatively), thereby maintaining the simplicity of mathematical and computational implementation and yielding precision comparable to those obtained by the Galerkin's method or the least square method. The degree of the B-spline approximation polynomial is instrumental in enhancing the precision of the method by allowing larger and better approximation and also by improving the accuracy at a larger number of knots.

To account for material and geometric nonlinearities associated with the problem and to enable a more comprehensive investigation, higher-order B-spline functions are employed. A custom MATLAB code has been developed to carry out the numerical analysis of the rotating FG beam.

3. Validation

The codes have been validated using different cases for natural frequencies of isotropic rotating and non-rotating beams and for FG rotating and non-rotating beams. The material composition of the considered FG beam is given in Table 1.

Case 1: In this case, a simply supported beam with $L = 0.5\,\mathrm{m}$, $h = 0.125\,\mathrm{m}$, composed of aluminium and steel is considered. The natural frequencies of the beam are compared with the results obtained from the present MATLAB code for both isotropic and functionally graded non-rotating beams, as shown in Table 2.

Case 2: A cantilever beam with parameters $L = 1\,\mathrm{m}$, $m = 6.4\,\mathrm{kg\,m^{-1}}$, $EI = 1.2\times10^5\,\mathrm{N\,m^2}$ is considered. Its natural frequencies for rotating and non-rotating case are presented in Table 3. The non-dimensional natural frequency and the non-dimensional rotational speed are given by

$$\bar{\omega} = \frac{\omega L^2}{h}\sqrt{\frac{\varrho_m}{E_m}}, \qquad \bar{\Omega} = \Omega L^2\sqrt{\frac{E_2}{\varrho_1}}.$$

Table 2. Natural frequencies of simply supported isotropic and FG beam [13]

$\bar{\omega}$	Pure steel	Present	$\lambda = 1$	Present	Pure aluminium	Present
1	6 728.89	6 729.653	6 457.93	6 458.663	6 615.66	6 616.415
2	22 279.03	22 278.85	21 603.18	21 603.01	21 904.14	21 903.97
3	41 094.04	41 093.80	40 145.42	40 145.18	40 402.57	40 402.33
4	6 0889.98	60 889.91	59 779.01	59 778.94	59 865.4	59 865.33
5	80 895.78	80 895.94	79 686.16	79 686.32	79 534.57	79 534.73

Table 3. Natural frequencies of a cantilever isotropic beam at non-dimensional rotational speed $\bar{\Omega} = \{0, 12\}$

Mode	$\bar{\Omega} = 0$		$\bar{\Omega} = 12$	
	Ref. [9]	Present	Ref. [9]	Present
1	3.516	3.512	13.170	13.167
2	22.034	22.002	37.603	37.544
3	61.697	61.477	79.614	79.320
4	120.90	120.109	140.535	139.602
5	199.86	197.781	220.539	218.232

The results obtained through the B-spline collocation shows good agreement with the previously accomplished work. The convergence test shown in Table 4 indicates that for $K = \{20, 25, 30, 35\}$, the obtained results do not change which implies that the value of $K = 20$ is sufficient for convergence.

4. Results and discussion

The present study analyses the dynamic behaviour of a rotating functionally graded (FG) beam composed of steel and alumina. The beam under consideration has a slenderness ratio of $L/h = 10$ and the shear correction factor

$$k_s = \frac{5(1+\mu)}{6+5\mu}$$

is applied to incorporate the effects of shear deformation. The other material properties of the FG beam, such as the Young's modulus, vary through the thickness according to the power-law distribution. The variation in the power index, rotational speed, slenderness ratio, and the effect of varying modulus ratio that govern the distribution of steel and alumina within the beam have been investigated.

Key non-dimensional parameters are defined to simplify the analysis and provide a generalised understanding of the beam behaviour. The rotational speed $\bar{\Omega}$, and the natural frequency $\bar{\omega}$ is given by

$$\bar{\omega} = \frac{\omega L^2}{h}\sqrt{\frac{\varrho_m}{E_m}}, \qquad \bar{\Omega} = \Omega L^2\sqrt{\frac{EA}{\varrho I}}, \qquad \text{where} \quad I = \frac{bh^3}{12}.$$

Table 4. The convergence properties of the first three natural frequencies at $\lambda = 1$ and $\bar{\Omega} = 2$

$\bar{\omega}$	$K = 10$	$K = 15$	$K = 20$	$K = 25$	$K = 30$
1	1.648	1.648	1.648	1.648	1.648
2	8.294	8.253	8.253	8.253	8.253
3	23.374	20.388	20.380	20.382	20.382
4	35.590	35.417	35.224	35.223	35.223

Table 5. Natural frequencies $\bar{\omega}$ for different power-law index λ of the functionally graded beam at $\bar{\Omega} = 5$, $L/h = 10$

$\bar{\omega}$	Power-law index λ							
	Ceramic	0.2	0.5	1	2	5	10	Metal
1	3.503	3.094	2.770	2.517	2.318	2.1362	2.034	0.976
2	13.325	11.760	10.512	9.527	8.7582	8.084	7.714	3.714
3	32.155	28.388	25.374	22.978	21.0947	19.4508	18.567	8.964
4	57.003	50.355	45.032	40.772	37.383	34.405	32.836	15.891
5	85.964	75.987	67.992	61.555	56.372	51.785	49.410	23.965
6	115.797	102.414	91.678	82.992	75.932	69.646	66.439	32.282
7	147.846	130.889	117.245	106.115	96.937	88.699	84.586	41.216
8	153.627	136.007	121.768	110.152	100.610	92.104	87.867	42.828
9	177.926	157.419	140.962	127.593	116.646	106.859	101.925	49.602
10	178.613	158.151	141.703	128.264	117.135	107.110	102.128	49.793

4.1. Effect of power-law index

The dynamic behaviour of functionally graded beam consisting of steel and aluminium is analysed at $L/h = 10$, where the beam is rotating at $\bar{\Omega} = 5$. The natural frequency of the beam is obtained at different values of the power-law index that regulates the distribution of steel and aluminium through the thickness of the beam. The resulting natural frequencies for this varying power-law index are shown in Table 5, which highlights the effects of material composition on the vibration properties of the beam. The results show a trend that offers an insight into the influence of material gradation on the dynamic behaviour of the beam. It is observed that the natural frequencies decrease as the power-law index increases, indicating a transition from pure ceramic to pure metal. This is due to the fact that ceramic materials (alumina) exhibit higher stiffness to density ratio as compared to metals, resulting in higher natural frequencies. As the power index increases, more steel is introduced into the beam, reducing stiffness while increasing the density. Lower stiffness leads to lower natural frequencies.

As we examine higher modes, the same decreasing trend can be seen. The higher modes are more sensitive to changes in material composition, which explains the more pronounced differences in natural frequencies at higher λ values. This behaviour reflects the fact that the natural frequency is directly related to the stiffness-to-density ratio of the beam. Alumina, with its higher stiffness, increases the beam natural frequencies, while steel, with a higher density and lower stiffness, reduces them. To examine the impact of the power-law index on the 1st, 2nd, 3rd, and 4th natural frequencies, graphs are presented in Fig. 3. Each plot depicts the variation of natural frequency with respect to the power index at different rotational speeds. As the rotational speed rises, its influence on each natural frequency becomes more significant, revealing unique patterns for each frequency mode. Fig. 3 shows a clear trend of decreasing natural frequency with an increase in power index. With an increase in the rotational speed, the value of the natural frequency also increases. The highest natural frequency is observed for $\lambda = 0$, as soon as the value of power index increases, the value of the natural frequency decreases up to a certain value of the power index.

For the first natural frequency, the decrease in natural frequency is observed up to $\lambda = 5$

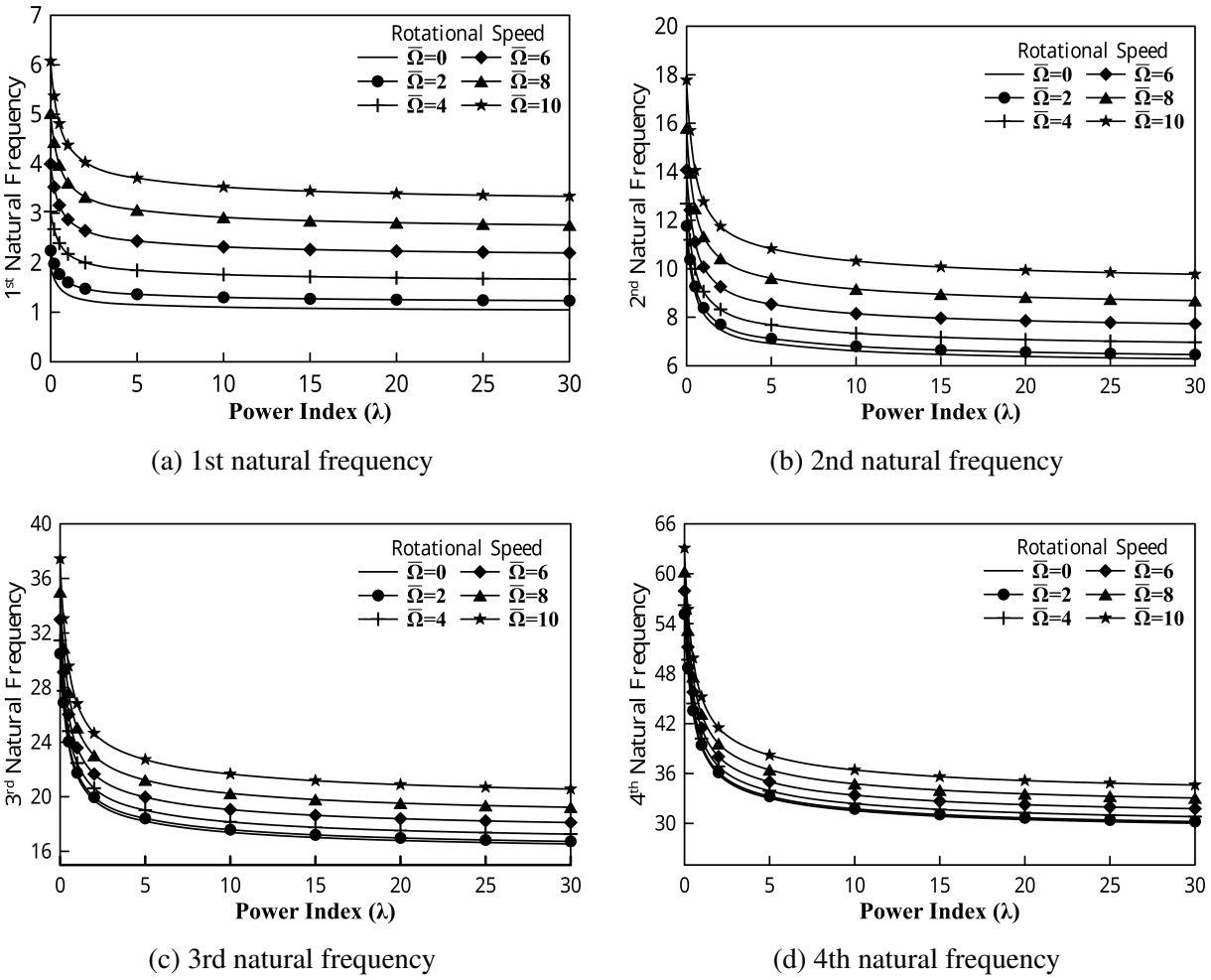

(a) 1st natural frequency

(b) 2nd natural frequency

(c) 3rd natural frequency

(d) 4th natural frequency

Fig. 3. Variation of natural frequencies with the power-law index λ at different values of $\bar{\Omega}$

and then the decrease is subtle and becomes almost constant from $\lambda = 15$. A similar trend is observed for the 2nd, 3rd, and 4th natural frequencies, where after $\lambda = 10$, the slope of the curve is low. At a lower speed, i.e., at $\bar{\Omega} = \{0, 2, 4\}$, the increase in the value of the natural frequency is low while it becomes more prominent for higher rotational speeds $\bar{\Omega} = \{6, 8, 10\}$. This trend is more notable for higher frequencies, i.e., for the 3rd and 4th natural frequencies.

4.2. Effect of rotational speed

The influence of the rotational speed on the natural frequency of the functionally graded rotating beam is obvious from Table 6. The slenderness ratio and the power index are considered as $L/h = 10$ and $\lambda = 1$, respectively, and the beam is rotated at various non-dimensional speeds. The listed data suggest that with increasing rotational speed $\bar{\Omega}$, the natural frequency also increases. This effect can be attributed to centrifugal stiffening, where the outward force generated by the rotation causes an increase in the effective stiffness. As the rotational speed $\bar{\Omega}$ increases, the centrifugal forces act to resist flexural deformations, resulting in higher natural frequencies. For example, at higher speeds (e.g., $\bar{\Omega} = 20$ or $\bar{\Omega} = 30$), the data show a noticeable increase in frequency values for each mode compared to lower speeds.

The relationship between the first four natural frequencies has been plotted against the rotational speed for three different power indexes $\lambda = \{0.2, 1, 2\}$ in Fig. 4. As the rotational

Table 6. Natural frequencies $\bar{\omega}$ for different values of the rotational speed $\bar{\Omega}$ of the functionally graded beam at $\lambda = 1$, $L/h = 10$

$\bar{\omega}$	Rotational speed $\bar{\Omega}$						
	0	5	10	15	20	25	30
1	1.357	2.517	4.376	6.298	8.231	10.168	12.109
2	8.156	9.527	12.764	16.775	21.095	25.560	30.100
3	21.517	22.978	26.823	32.087	38.098	44.512	51.146
4	39.158	40.772	45.200	51.571	59.113	67.345	75.989
5	59.825	61.555	66.488	73.881	82.794	92.677	103.286
6	81.008	82.992	88.964	98.098	108.583	119.587	131.787
7	102.677	106.115	115.494	127.394	134.987	145.209	158.544
8	108.151	110.152	116.347	128.822	143.847	153.707	165.813
9	124.790	127.593	130.787	136.17	153.150	156.848	179.512
10	126.521	128.265	138.206	153.342	172.210	174.587	196.999

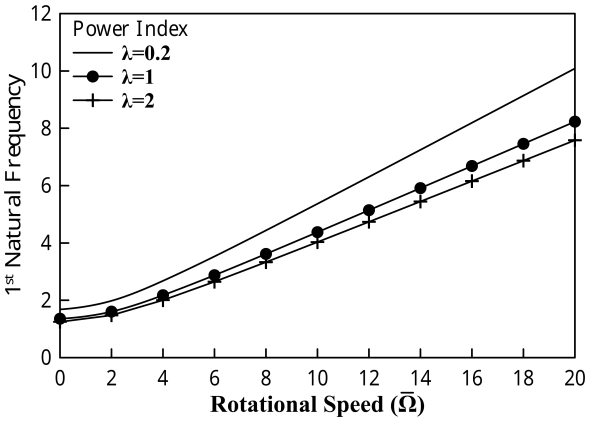

(a) 1st natural frequency

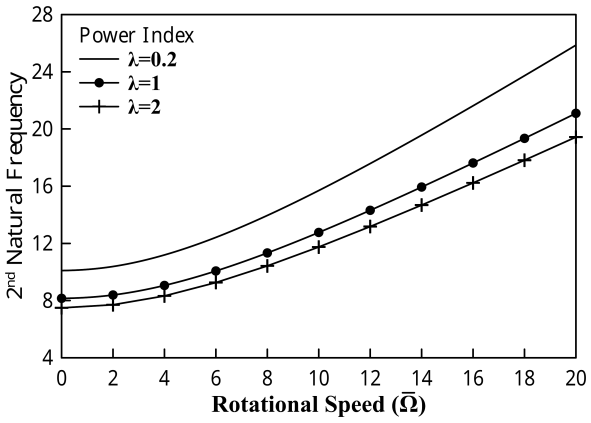

(b) 2nd natural frequency

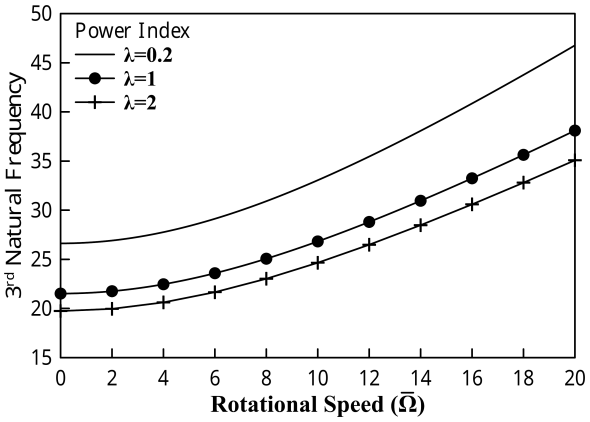

(c) 3rd natural frequency

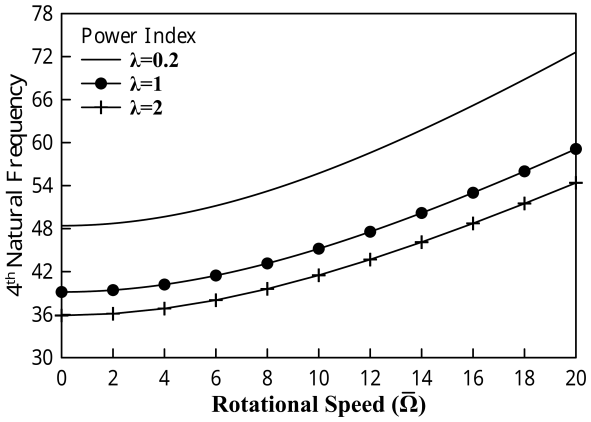

(d) 4th natural frequency

Fig. 4. Variation of natural frequencies with the rotational speed $\bar{\Omega}$ at different values of λ

speed increases, the natural frequency for all three power indexes increases at different rates. For lower rotational speeds, i.e., $\bar{\Omega} = 0 \div 4$, the proportion of increase in the natural frequency is low and increases rapidly at $\bar{\Omega} = 4$ onwards. For $\lambda = 0.2$, the highest natural frequency is obtained for all values of the rotational speed and for higher power indexes, the value of the natural frequency decreases due to reduced stiffness of the material. The deviation of natural frequency at different values of $\lambda = \{0.2, 1, 2\}$ increases with the mode number, i.e., for the 4th natural frequency (Fig. 4d). The highest deviation of the natural frequency between the power indexes is observed.

4.3. Effect of slenderness ratio

The correlation between the natural frequency and the slenderness ratio is shown in Table 7. At a constant rotational speed $\bar{\Omega} = 10$ and a power index of $\lambda = 1$, the natural frequency was observed in various slenderness ratios L/h ranging from 5 to 50. This dataset offers an insight into how changes in the slenderness ratio impact natural frequencies of the rotating FG beam for different modes (1 through 10). Higher slenderness ratios indicate a longer and slenderer beam relative to its thickness, making it more flexible and less resistant to bending and vibrational effects. At lower slenderness ratios, such as $L/h = 5$, the beam has a comparatively larger thickness, providing greater structural rigidity. Consequently, the natural frequencies across all the modes are lower compared to those in the case of higher slenderness ratios. The reason for this is because the thicker beam undergoes less bending and its stiffness is largely governed by its inherent material properties, rather than rotational stiffening. With an increasing slenderness ratio, the values of the natural frequency increase significantly for all modes. For example, for mode 1, the natural frequency increased from 4.297 at $L/h = 5$ to 4.409 at $L/h = 50$, although the increase is more pronounced in higher modes. This increase is due to the greater susceptibility of slender beams to centrifugal stiffening at higher rotational speeds.

Although the natural frequency generally increases with the increasing slenderness ratio, the rate of increase decreases as the slenderness ratio reaches higher values. This suggests that at very high slenderness ratios, the flexibility reaches a point where additional increases in L/h have minimal impact on the frequency. This behaviour implies that a threshold slenderness ratio

Table 7. Natural frequencies $\bar{\omega}$ at different values of slenderness ratio of rotating functionally graded beam for $\lambda = 1$, $\bar{\Omega} = 10$

$\bar{\omega}$	Slenderness ratio L/h						
	5	10	15	20	30	40	50
1	4.297	4.376	4.395	4.402	4.407	4.409	4.409
2	11.866	12.764	12.99	13.075	13.138	13.161	13.172
3	23.0561	26.823	28.001	28.482	28.852	28.988	29.052
4	35.975	45.2	48.691	50.244	51.500	51.974	52.201
5	49.559	66.489	73.950	77.562	80.652	81.862	82.448
6	62.773	88.965	101.475	107.975	113.828	116.206	117.378
7	69.597	115.49	135.096	145.426	148.337	140.716	135.374
8	72.540	116.35	136.346	148.825	154.937	158.811	135.374
9	76.379	130.79	150.024	154.376	161.595	167.367	160.711
10	82.315	138.21	165.691	182.422	195.952	187.503	170.371

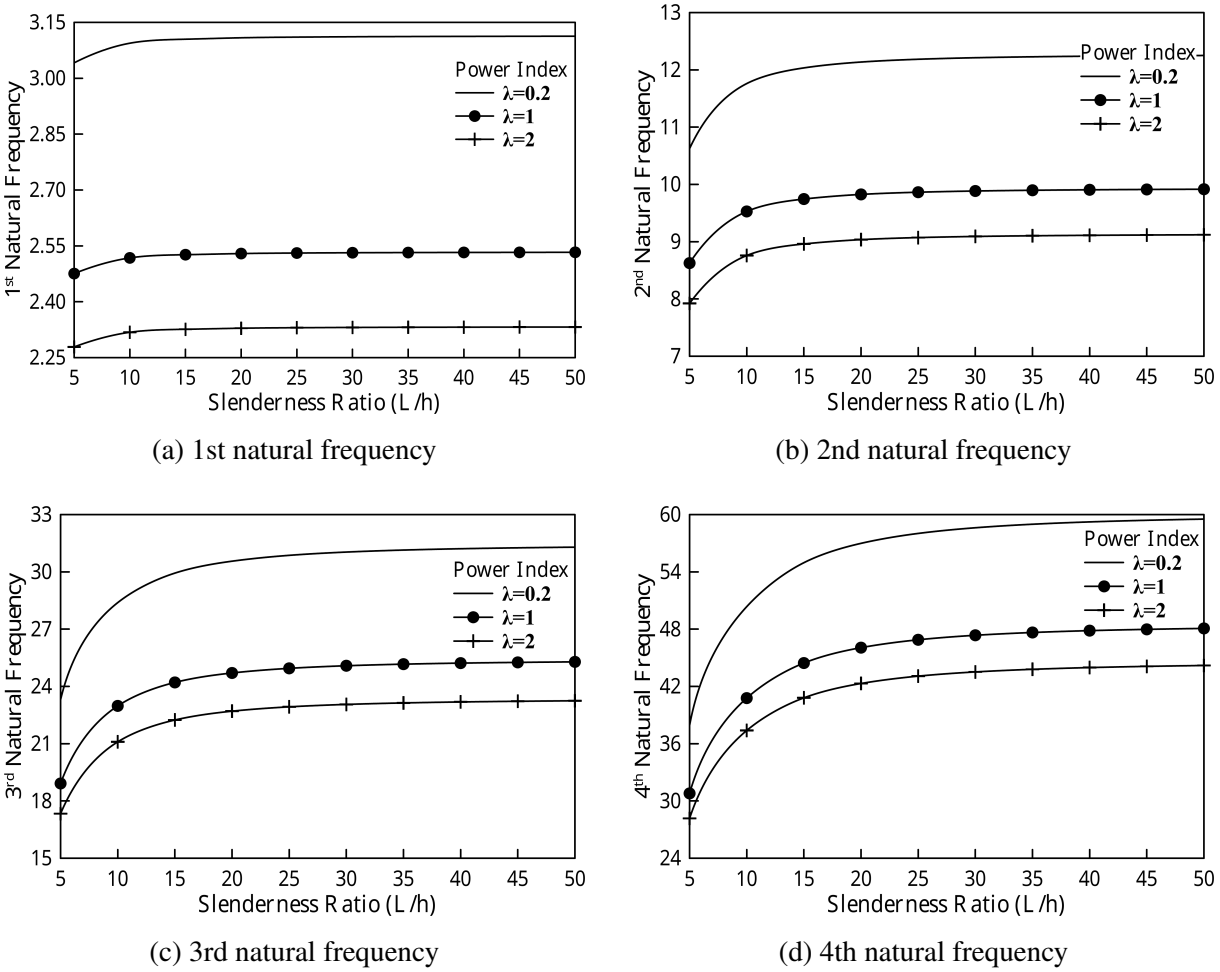

(a) 1st natural frequency

(b) 2nd natural frequency

(c) 3rd natural frequency

(d) 4th natural frequency

Fig. 5. Variation of natural frequencies with the slenderness ratio L/h for different values of λ and for $\bar{\Omega} = 5$

exists, beyond which the centrifugal stiffening effect contributes less to the frequency increase. Higher modes exhibit a greater sensitivity to changes in the slenderness ratio than the lower modes. This trend highlights those higher modes, which involve more complex vibrational patterns, and are more influenced by the geometric and rotational effects associated with the slenderness.

The natural frequencies of a rotating beam for four modes at a rotational speed $\bar{\Omega} = 10$ plotted against the slenderness ratio L/h for three power indices: $\lambda = \{0.2, 1, 2\}$ are shown in Fig. 5. As the slenderness ratio increases, the 1st natural frequency shown in Fig. 5a initially experiences a slight rise for all power indices, but this growth gradually levels off and tends toward an asymptotic value. This behaviour suggests that beyond a certain slenderness ratio, further increases have a negligible effect on the 1st natural frequency. The initial rise is due to the increased flexibility associated with a higher L/h ratio, which makes the beam more responsive to centrifugal stiffening effects at the initial stage. However, as the beam becomes very slender, this effect saturates and further changes in L/h have limited impact. For the 2nd, 3rd, and 4th natural frequencies, Figs. 5b–d show the same trend of an increase in the natural frequency with an increase in the slenderness ratio. However, the rate of increase in the natural frequency increases with the mode number, and the 4th natural frequency displays a more pronounced increase with the slenderness ratio, particularly at lower values of L/h.

Table 8. Natural frequencies $\bar{\omega}$ at different material composition of rotating functionally graded beam for $\bar{\Omega} = 10$

Material composition	$\bar{\omega}$	Power-law index λ				
		0.2	0.5	1	2	5
Steel/Aluminium	1	3.208	3.191	3.230	3.341	3.482
	2	9.383	9.299	9.355	9.626	10.049
	3	19.766	19.545	19.565	20.023	20.880
	4	33.354	32.981	32.951	33.594	34.897
	5	49.107	48.591	48.510	49.314	51.002
Aluminium/Alumina	1	5.785	5.429	5.129	4.892	4.892
	2	16.905	15.748	14.686	13.822	13.822
	3	35.592	32.995	30.445	28.294	28.294
	4	60.051	55.629	51.137	47.222	47.222
	5	88.423	81.964	75.257	69.234	69.234
Zirconia/Alumina	1	3.275	3.259	3.262	3.282	3.296
	2	9.585	9.535	9.536	9.587	9.629
	3	20.191	20.079	20.067	20.155	20.234
	4	34.042	33.853	33.814	33.927	34.030
	5	50.073	49.799	49.719	49.836	49.941

Although it eventually normalises, the rate of increase and the final frequency values are significantly higher compared to the 1st natural frequency. This suggests that higher modes are more sensitive to changes in the slenderness ratio. The dimensionless natural frequencies $\bar{\omega}$ for a rotating beam made from three different combinations of FGM, in particular steel/aluminium (steel/Al), aluminium/aluminium (Al/Al_2O_3), and zirconia/aluminium (Zr/Al_2O_3), with a rotational speed of $\bar{\Omega} = 10$ and various power indexes λ are listed in Table 8. Since the stiffer material forms the upper surface, increasing power index leads to a higher volume fraction of metal, which lowers the stiffness. Therefore, aluminium/alumina FGM displays a notable decrease in natural frequencies as the power index increases, with values decreasing steadily across all the modes from 0.2 to 5 due to a higher stiffness ratio. However, for the zirconia/alumina combination, the natural frequencies remain almost constant across all the values of λ, showing minimal variation. Both zirconia and alumina are ceramics with similar stiffness values, so changes in their proportion have a limited effect on the overall stiffness of the beam.

However, in the case of steel/aluminum, the natural frequency increases with the power-law index due to the rising volume fraction of aluminum. The effect is more prominent in higher modes due to the increasing sensitivity of higher-frequency modes to changes in stiffness and material composition.

The 1st and 4th natural frequencies for the three types of above-mentioned FGMs are plotted against the power index λ in Fig. 6. The 1st natural frequency in Fig. 6a shows that for aluminium/alumina the frequency decreases significantly as λ increases from 0.5 to 5. This is probably due to a decrease in the stiffness as the volume fraction of aluminium increases, which is a less stiff material compared to alumina. Steel/aluminium has a subtle increase in natural frequency with increasing λ from 0.5 to 5, which implies that its structural behaviour is less sensitive to compositional changes in the considered range of λ. Steel and aluminium

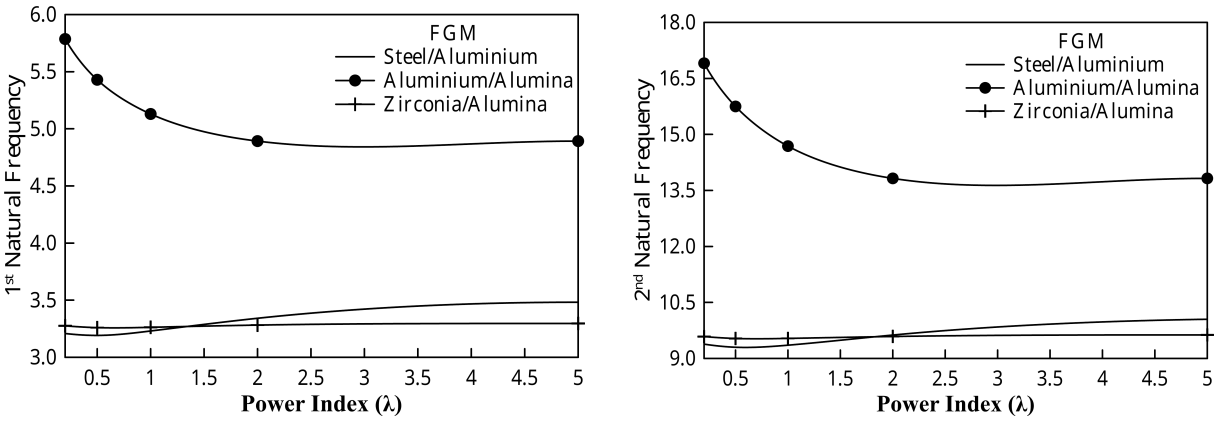

(a) 1st natural frequency

(b) 2nd natural frequency

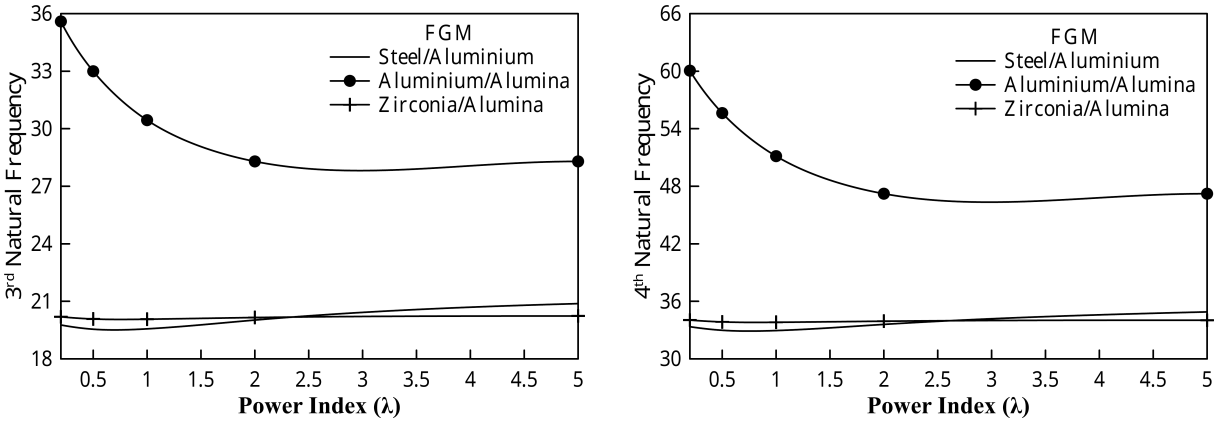

(c) 3rd natural frequency

(d) 4th natural frequency

Fig. 6. Variation of the natural frequencies with the power index λ for $\bar{\Omega} = 10$ for different material compositions

have densities and stiffness ratios more similar to ceramics such as alumina. Zirconia/alumina shows a very slight increase in frequency with λ, remaining relatively constant. This is because both zirconia and alumina are ceramics with similar stiffness, so their gradation does not greatly impact the natural frequencies.

Moving toward the higher frequencies, i.e., the 2nd, 3rd, and 4th natural frequencies in Figs. 6b–d, the trends mirror those seen in the 1st natural frequency but with higher magnitude differences. The responsiveness of natural frequencies to the power index is primarily affected by the inconsistency in constituent material properties, with metal/ceramic based FGMs exhibiting more frequency variation due to higher differences in material properties compared to metal/metal and ceramic/ceramic based FGMs.

5. Conclusion

The dynamic analysis of rotating functionally graded (FG) beams is crucial to understanding their vibration characteristics under different operating conditions. This paper focuses on evaluating the dynamic response of a rotating FG beam. The results indicate that parameters such as the rotational speed, slenderness ratio, and material composition influence the natural frequencies differently due to the effects of material gradation.

1. The power-law index substantially affects the dynamic behaviour of the rotating FG beam, with a higher ceramic content resulting in stiffer, higher frequency beams, whereas a higher metal content lowers the stiffness and the corresponding natural frequencies. The used material composition of steel/alumina shows that the natural frequency of the rotating beam is directly proportional to the stiffness to mass ratio of the beam.
2. Incorporating rotational speed will result in centrifugal stiffening of the beam, which in turn increases the natural frequency. For a given value of the power-law index, increasing rotational speed increases natural frequency. The rate of increase in natural frequency is higher at a lower mode, while lower for a higher mode.
3. As the slenderness ratio increases, the natural frequency tends to rise, primarily due to the centrifugal stiffening effect in the rotating beam. However, this increase saturates at higher ratios, particularly at lower modes. Higher modes show a greater response to the slenderness ratio, suggesting that they are more influenced by geometric changes of the beam.
4. The influence of the power index on the natural frequency depends on the difference in properties between the materials used in the FGM. FGMs with contrasting properties of metal/ceramic (such as aluminium/alumina) show significant changes, while FGMs with similar metal/metal and ceramic/ceramic materials (such as steel/alumina and zirconia/alumina) exhibit uniformity across the power index range.

Acknowledgement

The authors gratefully acknowledge National Institute of Technology, Raipur for their support and providing platform for this research.

References

[1] Almitani, K. H., Eltaher, M. A., Abdelrahman, A. A., Abd-El-Mottaleb, H. E., Finite element based stress and vibration analysis of axially functionally graded rotating beams, Structural Engineering and Mechanics 79 (1) (2021) 23–33. https://doi.org/10.12989/sem.2021.79.1.023

[2] Banerjee, J. R., Dynamic stiffness formulation and free vibration analysis of centrifugally stiffened Timoshenko beams, Journal of Sound and Vibration 247 (1) (2001) 97–115. https://doi.org/10.1006/jsvi.2001.3716

[3] Bouzidi, I., Hadjoui, A., Fellah, A., Dynamic analysis of functionally graded rotor-blade system using the classical version of the finite element method, Mechanics Based Design of Structures and Machines 49 (7) (2021) 1 080–1 108. https://doi.org/10.1080/15397734.2019.1706558

[4] Chen, Y., Guo, X., Zhang, D., Li, L., Dynamic modeling and analysis of rotating FG beams for capturing steady bending deformation, Applied Mathematical Modelling 88 (2020) 498–517. https://doi.org/10.1016/j.apm.2020.06.035

[5] Ebrahimi, F., Dashti, S., Free vibration analysis of a rotating non-uniform functionally graded beam, Steel and Composite Structures 19 (5) (2015) 1 279–1 298. https://doi.org/10.12989/scs.2015.19.5.1279

[6] Ebrahimi, F., Mokhtari, M., Free vibration analysis of a rotating Mori-Tanaka-Based functionally graded beam via differential transformation method, Arabian Journal for Science and Engineering 41 (2) (2016) 577–590. https://doi.org/10.1007/s13369-015-1689-7

[7] Ebrahimi, F., Mokhtari, M., Vibration analysis of spinning exponentially functionally graded Timoshenko beams based on differential transform method, Proceedings of the Institution of Mechanical Engineers, Part G: Journal of Aerospace Engineering 229 (14) (2015) 2 559–2 571. https://doi.org/10.1177/0954410015580801

[8] Fang, J. S., Zhou, D., Free vibration analysis of rotating axially functionally graded tapered Timoshenko beams, International Journal of Structural Stability and Dynamics 16 (5) (2016) 1–19. https://doi.org/10.1142/S0219455415500078

[9] Gunda, J. B., Ganguli, R., New rational interpolation functions for finite element analysis of rotating beams, International Journal of Mechanical Sciences 50 (3) (2008) 578–588. https://doi.org/10.1016/j.ijmecsci.2007.07.014

[10] Hao-Nan, L., Cheng, L., Ji-Ping, S., Lin-Quan, Y., Vibration analysis of rotating functionally graded piezoelectric nanobeams based on the nonlocal elasticity theory, Journal of Vibration Engineering and Technologies 9 (6) (2021) 1 155–1 173. https://doi.org/10.1007/s42417-021-00288-9

[11] Karahan, E. D., Özdemir, Ö., Finite element formulation and free vibration analyses of rotating functionally graded blades, Journal of Theoretical and Applied Mechanics 59 (1) (2021) 3–15. https://doi.org/10.15632/jtam-pl/127537

[12] Kılıç, B., Özdemir, Ö., Vibration and stability analyses of functionally graded beams, Archive of Mechanical Engineering 68 (1) (2021) 93–113. https://doi.org/10.24425/ame.2021.137043

[13] Li, X. F., A unified approach for analyzing static and dynamic behaviors of functionally graded Timoshenko and Euler-Bernoulli beams, Journal of Sound and Vibration 318 (4–5) (2008) 1 210–1 229. https://doi.org/10.1016/j.jsv.2008.04.056

[14] Nguyen, T.-K., Vo, T. P., Thai, H. T., Static and free vibration of axially loaded functionally graded beams based on the first-order shear deformation theory, Composites Part B: Engineering 55 (2013) 147–157. https://doi.org/10.1016/j.compositesb.2013.06.011

[15] Özdemir, Ö., Vibration analysis of rotating Timoshenko beams with different material distribution properties, Selcuk University Journal of Engineering, Science and Technology 7 (2) (2019) 272–286. https://doi.org/10.15317/scitech.2019.198

[16] Ozdemir Ozgumus, O., Kaya, M. O., Vibration analysis of a rotating tapered Timoshenko beam using DTM, Meccanica 45 (1) (2010) 33–42. https://doi.org/10.1007/s11012-009-9221-3

[17] Panchore, V., Ganguli, R., Quadratic B-spline finite element method for a rotating nonuniform Euler-Bernoulli beam, International Journal for Computational Methods in Engineering Science and Mechanics 19 (5) (2018) 340–350. https://doi.org/10.1080/15502287.2018.1520757

[18] Piovan, M. T., Sampaio, R., A study on the dynamics of rotating beams with functionally graded properties, Journal of Sound and Vibration 327 (1–2) (2009) 134–143. https://doi.org/10.1016/j.jsv.2009.06.015

[19] Şimşek, M., Fundamental frequency analysis of functionally graded beams by using different higher-order beam theories, Nuclear Engineering and Design 240 (4) (2010) 697–705. https://doi.org/10.1016/j.nucengdes.2009.12.013

[20] Thomas, O., Sénéchal, A., Deü, J.-F., Hardening/softening behavior and reduced order modeling of nonlinear vibrations of rotating cantilever beams, Nonlinear Dynamics 86 (2) (2016) 1 293–1 318. https://doi.org/10.1007/s11071-016-2965-0

[21] Wattanasakulpong, N., Prusty, B. G., Kelly, D. W., Hoffman, M., Free vibration analysis of layered functionally graded beams with experimental validation, Materials & Design 36 (2012) 182–190. https://doi.org/10.1016/j.matdes.2011.10.049

[22] Zghal, S., Ataoui, D., Dammak, F., Free vibration analysis of porous beams with gradually varying mechanical properties, Proceedings of the Institution of Mechanical Engineers Part M: Journal of Engineering for the Maritime Environment 236 (3) (2022) 800–812. https://doi.org/10.1177/14750902211047746